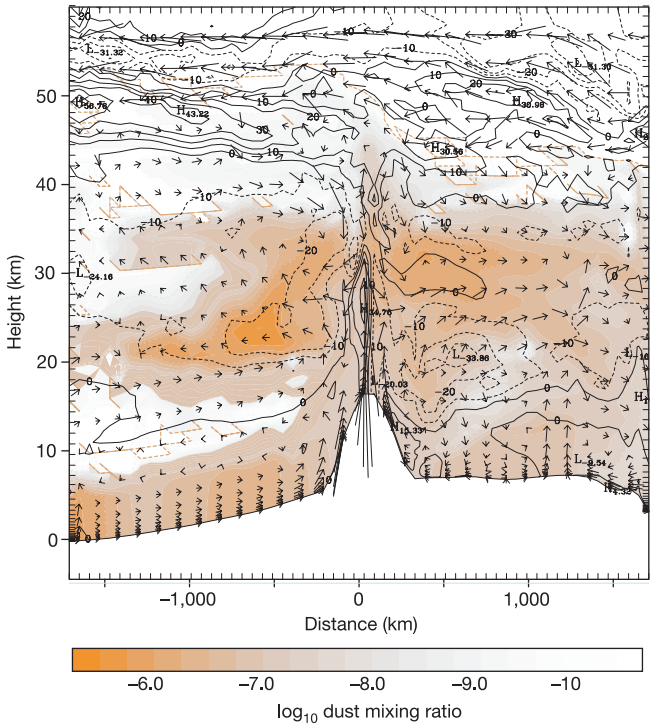

Figure 4 A vertical, east–west cross-section from grid two, cutting through the centre of Arsia Mons. Shaded regions are $\log_{10}$ of the dust mixing ratio. Contour lines indicate meridional wind: solid lines, northward-moving air (into the page); dotted lines, southward-moving air (out of the page). Vectors indicate wind velocity in the plane of the figure. The maximum horizontal wind speed is 95 m s^{-1}. The maximum vertical velocity is 9 m s^{-1}. The dust takes the form of a mushroom-shaped cloud. The upper-level outflow from the thermal circulation advects the dust more than 2,000 km downwind. The meridional wind shows a tight clockwise rotation directly above the caldera. The outflow region to either side of the volcano exhibits a weaker anticlockwise rotation.

(not shown). It would not be unexpected for a water-ice cloud to develop at the top of the thermal circulation. Such cap clouds have been observed by the MOC and by the Viking orbiter[12]. But the actual amount of water vapour in the air is unknown, so we chose to run the model without the presence of any water substance in this study.

The GCMs that are typically used to study the climate of Mars have too coarse a grid spacing to properly resolve Arsia Mons (or the other volcanoes, all of which exhibit similar circulations), and are therefore unable to capture the magnitude of the thermal circulation or the dust injection mechanism associated with the circulations. These same models would not properly reproduce the radiative balance of the atmosphere, as they would not reproduce the dust loading. The easterly winds in the outflow branch (Fig. 4) effectively enhance the depth of the upper-level large-scale easterly winds. Westerly winds in the outflow located below the large-scale upper-level easterly winds increase the wind shear. Consequently, the thermal circulation creates a large perturbation in the larger-scale momentum and thermal fields.

Mars is dotted with numerous topographic features that are too small in horizontal extent to be captured by GCMs, but which may produce large-scale thermal circulations that could perturb the general circulation. Our results suggest that mesoscale thermal circulations may collectively be important in the atmospheric dust budget, and individually can produce strong regional perturbations in the background large-scale flow. □

Received 10 April; accepted 10 September 2002; doi:10.1038/nature01114.

1. Cantor, B., Malin, M. & Edgett, K. S. Multiyear Mars Orbiter Camera (MOC) observations of repeated Martian weather phenomena during the northern summer season. *J. Geophys. Res.* **107,** 10.1029/2001JE001588 (2002).
2. Cantor, B. A., James, P. B., Caplinger, M. & Wolff, M. J. Martian dust storms: 1999 Mars Orbiter Camera observations. *J. Geophys. Res.* **106,** 23653–23687 (2002).
3. Malin, M. C. & Edgett, K. S. Mars Global Surveyor Mars Orbiter Camera: Interplanetary cruise through primary mission. *J. Geophys. Res.* **106,** 23429–23570 (2001).
4. Haberle, R. M. *et al.* General circulation model simulations of the Mars Pathfinder atmospheric structure investigation/meteorology data. *J. Geophys. Res.* **104,** 8597–8974 (1999).
5. Wilson, R. J. & Hamilton, K. Comprehensive model simulation of thermal tides in the Martian atmosphere. *J. Atmos. Sci.* **53,** 1290–1326 (1996).
6. Forget, F. *et al.* Improved general circulation models of the Martian atmosphere from the surface to above 80 km. *J. Geophys. Res.* **104,** 24155–24175 (1999).
7. Rafkin, S. C. R., Haberle, R. M. & Michaels, T. I. The Mars Regional Atmospheric Modeling System (MRAMS): Model description and selected simulations. *Icarus* **151,** 228–256 (2001).
8. Tyler, D., Barnes, J. R. & Haberle, R. M. Simulation of surface meteorology at the Pathfinder and VL1 sites using a Mars mesoscale model. *J. Geophys. Res.* 10.1029/2001JE001618 (2002).
9. Toigo, A. D. & Richardson, M. I. A mesoscale model for the Martian atmosphere. *J. Geophys. Res.* **107,** 10.1029/2001JE001489 (2002).
10. Pielke, R. A. *et al.* A comprehensive meteorological modeling system—RAMS. *Meteorol. Atmos. Phys.* **49,** 69–91 (1992).
11. Murphy, J. R., Haberle, R. M., Toon, O. B. & Pollack, J. B. Martian global dust storms: Zonally symmetric numeric simulations including size-dependent particle transport. *J. Geophys. Res.* **98,** 3197–3220 (1993).
12. Hunt, G. E., Pickersgill, A. O., James, P. B. & Johnson, G. Some diurnal properties of clouds over the martian volcanoes. *Nature* **286,** 362–364 (1980).

Acknowledgements We thank Malin Space Science Systems and M. Malin for permitting the use of MOC imagery before release on Planetary Data System. We also thank A. Bridger for comments and suggestions. This work was supported by the NASA Planetary Atmosphere Program, the Mars Data Analysis Program and the Mars Global Surveyor Data Analysis Program.

Competing interests statement The authors declare that they have no competing financial interests.

Correspondence and requests for materials should be addressed to S.C.R.R. (e-mail: rafkin@metsun1.met.sjsu.edu or srafkin@boulder.swri.edu).

Cavity solitons as pixels in semiconductor microcavities

Stephane Barland*¶, Jorge R. Tredicce*¶, Massimo Brambilla†¶, Luigi A. Lugiato‡, Salvador Balle§, Massimo Giudici*, Tommaso Maggipinto†, Lorenzo Spinelli‡, Giovanna Tissoni‡, Thomas Knödl‖, Michael Miller‖ & Roland Jäger‖

* *Institut Non Lineaire de Nice, 1361 Route des Lucioles, F-06560 Valbonne, France*
† *INFM, Dipartimento di Fisica Interateneo, Poltecnico e Università di Bari, Via Orabona 4, 70126 Bari, Italy*
‡ *INFM, Dipartimento di Scienze, Università dell'Insubria, Via Valleggio 11, 22100 Como, Italy*
§ *IMEDEA, Carrer Miguel Marques 21, 07190 Esporles, Islas Baleares, Spain*
‖ *Department of Optoelectronics, University of Ulm, Albert-Einstein-Allee 45, D-89069 Ulm, Germany*
¶ *These authors contributed equally to this work*

Cavity solitons are localized intensity peaks that can form in a homogeneous background of radiation. They are generated by shining laser pulses into optical cavities that contain a nonlinear medium driven by a coherent field (holding beam). The ability to switch cavity solitons on and off[1,2] and to control their location and motion[3] by applying laser pulses makes them interesting as potential 'pixels' for reconfigurable arrays or all-optical processing units. Theoretical work on cavity solitons[2–7] has stimulated a variety of experiments in macroscopic cavities[8–10] and in systems with optical feedback[11–13]. But for practical devices, it is desirable to generate cavity solitons in semiconductor structures, which

would allow fast response and miniaturization. The existence of cavity solitons in semiconductor microcavities has been predicted theoretically[14–17], and precursors of cavity solitons have been observed, but clear experimental realization has been hindered by boundary-dependence of the resulting optical patterns[18,19]—cavity solitons should be self-confined. Here we demonstrate the generation of cavity solitons in vertical cavity semiconductor microresonators that are electrically pumped above transparency but slightly below lasing threshold[20]. We show that the generated optical spots can be written, erased and manipulated as objects independent of each other and of the boundary. Numerical simulations allow for a clearer interpretation of experimental results.

Arrays of cavity solitons (CSs) are nonlinear optical structures[21] within which independent manipulation of the intensity peaks is possible. Cavity solitons belong to the class of localized structures, which also exist in other fields (see, for example, ref. 22), and arise under conditions of coexistence of a homogeneous stationary state and a patterned stationary state for the same values of parameters. Localized structures coincide with the pattern state in a certain restricted region of the plane, and with the homogeneous state outside. A CS corresponds to a localized structure with a single peak. Once 'written' by injecting a laser pulse, the CS can be 'erased' by injecting another pulse, out of phase with respect to the holding beam, in the location where the CS lies[2]. In the presence of a phase or intensity modulation in the holding beam, CSs tend to move to the nearest local maximum of the modulated profile[3].

Our experimental set-up is schematically shown in Fig. 1. It consists of a large-area vertical cavity surface emitting laser (VCSEL, 150 μm diameter), operated as an amplifier; injected into this laser is a coherent field, generated by a high-power edge emitting laser with an external cavity grating. Its wavelength can be continuously tuned in the range 960–980 nm. An acousto-optic modulator or a polarizer controls the external field intensity. The VCSEL is a bottom emitter[23]. One of the electrodes is deposited on the top, covering the whole transverse size of the laser. A full-area n-type contact with a circular emission window is deposited at the back of the GaAs substrate. The large distance between this ring and the active medium ensures a better uniformity of the current than in the case of top-emitter lasers.

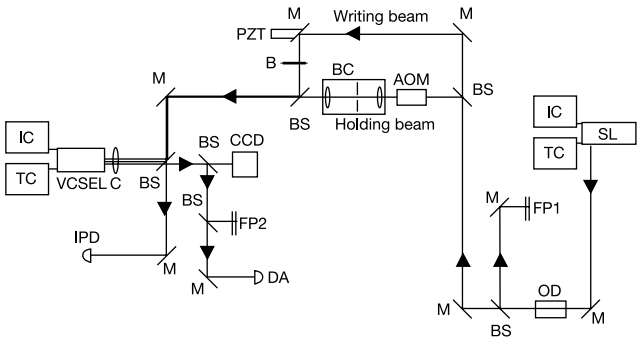

Figure 1 Schematic experimental set-up. SL, high-power edge emitter laser; its frequency is controlled by means of a grating. IC, current stabilization; the overall current is stabilized better than 1‰. TC, temperature controller. A Peltier junction ensures thermal stabilization of better than 0.01 °C. OD, optical diode to isolate the laser producing the holding beam from optical feedback. FP1, FP2, Fabry–Perot resonators that measure the optical frequency of the holding and writing beams (FP1) and output beam (FP2). FP2 is coupled to a fibre in order to measure the spatially resolved optical spectra. The free spectral range (FSR) is 140 GHz, and the finesse is 100. AOM, acousto-optic modulator to change the intensity of the holding beam. BC, beam expander-configurator, used to enlarge and to conform the holding beam. VCSEL, broad-area (150 μm) vertical cavity surface emitting laser. C, collimator. CCD, charge-coupled-device camera used to monitor the time-averaged intensity distribution (near field) of the beam reflected by the VCSEL and of the holding beam. IPD, photo-detector to measure the intensity of the holding and writing beams. DA, detector array allowing simultaneous measurement of the intensity at different points of the transverse pattern. PZT, piezo-electric ceramic used to change the phase of the writing beam relative to the holding beam. B, blocker. M, mirrors. BS, beam-splitters. The transverse intensity distribution of the master oscillator is spatially filtered and shaped by lenses. Its amplitude is monitored by a photodiode and its optical frequency analysed by a Fabry–Perot interferometer with a free spectral range of 2.5 THz and a finesse of 140. An optical isolator is used to avoid feedback from the sample into the master oscillator.

We used numerous samples, progressing in time towards optimization of the device architecture. Broad-area VCSELs usually exhibit a strong gradient of the cavity length along the transverse section, owing to the standard epitaxial growth techniques. It is important to note that the output intensity distribution of the free-running VCSEL is not strictly uniform. At currents around 180 mA, the intensity distribution can be associated with a Gauss–Laguerre TEM_{0n} mode (Fig. 2a), with n of the order of 30 or larger, which implies that the system is able to operate with a very large Fresnel number. An analysis of the spatially resolved optical spectrum (Fig. 2b) indicates that the free-running laser emits several frequencies, and that the spectral composition varies with the spatial position across the sample. We can also conclude that the centre region of the VCSEL behaves independently of the boundaries, and hence that the spatial correlation length is much smaller than the size of the sample.

Operating at current values for which the centre region is below threshold, we now inject a coherent holding field: the spatial intensity output distribution undergoes marked changes in that region, while the region near the boundary remains qualitatively unchanged. We estimate that the boundaries control the characteristics of the pattern over distances of around 10 μm. A homogeneous low-intensity region appears on the right-hand side of the sample (Fig. 2c). It is delimited by a well-defined line formed by several high-intensity spots, orthogonal to the cavity resonance gradient. On the left of that line, we see a pattern whose spatial wavelength decreases as it approaches the boundary layer. The

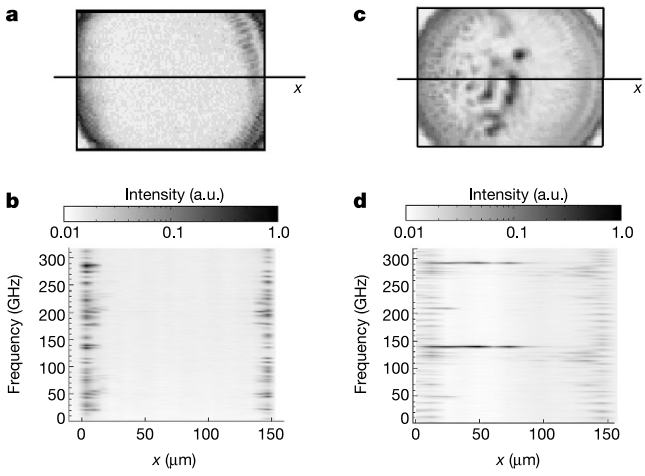

Figure 2 Average intensity distribution and spatially resolved power spectra (along the lines labelled x in **a** and **c**) for the free running laser (FRL) and for the driven VCSEL. **a**, **b**, The intensity distribution (**a**) and the spectrum (**b**) for the FRL pumped at 300 mA. Emission at several well-defined frequencies is observed near the boundary. **c**, **d**, The intensity distribution (**c**) and the spectrum (**d**) for the VCSEL with injected field. The darker lines (high intensity) in **d** correspond to the frequency of the injected field. The frequency interval between the two dark lines in **d** corresponds to the free spectral range of the Fabry–Perot resonator. The region close to the boundary still shows emission at several frequencies, while the centre region is locked at the frequency of the external field. No defined frequency is observed in the homogeneous region because the intensity is not high enough to allow a measurement with the sensitivity of our detectors.

transition from a homogeneous to a patterned region can be understood by considering that the detuning between cavity resonance and the frequency of the external field is changing along the gradient, and that pattern formation favours larger blue detunings. The spatially resolved optical spectrum (Fig. 2d) shows several frequencies close to the transverse boundary of the VCSEL. However, beyond the boundary layer, the dominant frequency becomes that of the injected field—that is, the VCSEL is locked to the master oscillator. The line separating the pattern and the homogeneous field phase can be interpreted as the locus of the spatial positions where the local values of the cavity resonance and field intensity meet the condition for the onset of a pattern-inducing modulational instability[21].

This interpretation is supported by our theoretical analyses and simulations, which are based on the model formulated in ref. 16 and generalized to take into account the following: the spatial profile of the holding beam and of the electric current, the constant gradient in cavity resonance, and the unavoidable irregularities in the layers of the Bragg reflectors. The gradient implies that the cavity detuning parameter θ varies uniformly along the sample. Figure 3 shows that the line that marks the instability boundary corresponds precisely to the line that separates the pattern and the homogeneous region in the sample.

Fixing all parameter values (amplitude and frequency of the external field and pumping current), we inject a small focused beam (the writing beam) into the homogeneous region. Starting with no spot, the writing beam is capable of generating a high-intensity spot with a diameter of the order of 10 μm when it is in phase with the holding beam. If we remove the writing beam, the bright spot remains 'on' indefinitely. We then change the writing beam phase by π, and inject it again into the sample where the bright spot is. The spot disappears. We remove the writing beam again, and the spatial intensity distribution becomes the same as it was at the beginning of the experiment. This proves that we can optically manipulate a single spot, which we claim to be a cavity soliton. Injecting a writing beam in a slightly different location, we can generate a CS: but after removal of the writing beam, it is found to be at the position of the previous spot, suggesting that the latter spot is an attracting locus for CSs. This experiment was repeated at several values of the pumping current between 320 and 360 mA.

By changing the frequency of the injected field, we find various positions where a CS can be located, always to the right of the limit between the homogeneous state and the pattern. Thus, such structures exist in a relatively wide range of injected field intensity and/or pumping current, and always close to the critical detuning value corresponding to the modulational instability. The fact that only a single stable soliton location can exist for fixed parameters is attributed to the presence of the strong resonance gradient. This acts as 'wind', which tends to blow the CS (with a velocity proportional to the gradient) out of its existence region. Thus we can observe a stationary spot only if we can vectorially compensate the force exerted by the cavity length gradient by a force exerted by an intensity gradient of the holding beam, which tends to attract the CS towards the beam centre. Such a compensation can occur only in one spatial position in the transverse plane.

In order to show that more than one spot can be manipulated independently (and therefore that we can definitively identify them as cavity solitons) for a fixed set of the operational parameters, we

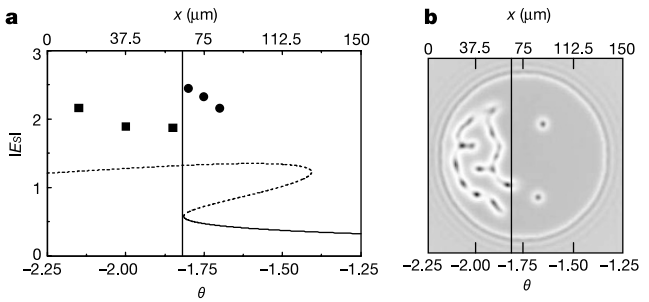

Figure 3 Numerical simulation and theoretical interpretation of the spatial field profile. **a**, The stable (solid) and unstable (broken) portions of the curve of the intracavity field versus the cavity detuning parameter θ, in the homogeneous stationary solution as proceeding from an analytical evaluation of the pattern-inducing modulational instability. It follows from a linear stability analysis of the model equations under plane wave holding field and flat current profile. Such approximations are reasonably met in the central region of the sample. The stable part of the plane-wave stationary curve terminates at $\theta = -1.81$, which corresponds to the instability boundary; it is shown by the vertical line. On the left of the line are patterns whose maximum intensities are indicated by squares. On the right, where the homogeneous background is still stable, CSs can be excited (maximum intensities marked by circles). **b**, The numerical transverse field intensity profile. The lower and upper scales indicate the value of θ that corresponds to each coordinate x. The vertical line in **b** corresponds to that in **a**; it can be seen that it satisfactorily meets the actual boundary of the patterned region. Two CSs are excited in the homogeneous region by applying two 6-ns pulses at delayed times. In the following evolution (90 ns), the two CSs move under the combined influence of the detuning gradient and the imperfections, for less than 30 ns, and are eventually pinned in the two locations (just a few micrometres away from where the switching beams were addressed). This simulation includes a time averaging comparable (1 μs) to that of the CCD used in the experiments (Fig. 4).

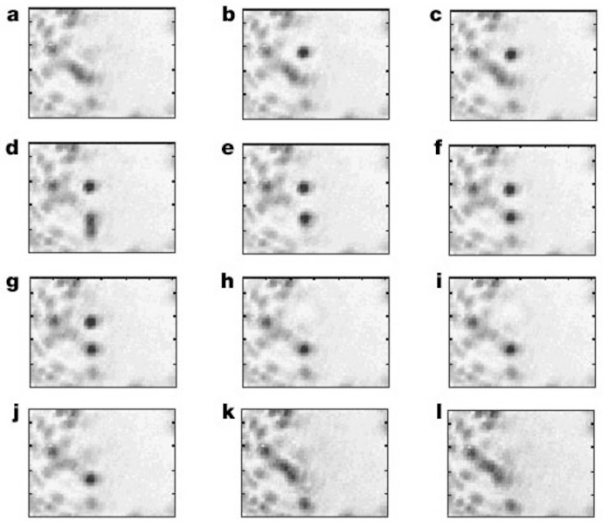

Figure 4 Experimental demonstration of independent writing and erasing of CSs. The intensity distribution of the output field is shown over a 60 μm × 60 μm region in the sample centre. The holding beam is always on, with a waist ranging from 150 to 250 μm with no significant effect; all other parameters are kept constant. The writing beam power is approximately 50 μW and the holding beam power is 8 mW, although no optimization of such values have been attempted. The persistency of the excited CSs exceeds the observation time (>1 min.). **a**, The writing beam (WB) is blocked. **b**, The 15-μm focused WB impinges on the homogeneous region; it induces the appearance of a single high-intensity spot (dark in the figure) in a limited region of space; **c**, the WB is blocked again, a 10-μm spot remains and is stable; **d**, the WB is displaced in position and switched on again. It generates a second spot; **e**, **f**, the WB is blocked again and the two bright spots coexist; **g**, the WB is positioned again on the first spot; **h**, the relative phase of the WB relative to the holding beam is changed by π, and the upper spot disappears; **i**, the WB is blocked again, the lower spot persists undisturbed; **j**, the WB is switched on again at the position of the lower spot; **k**, the relative phase of the WB is again brought to π and also the second spot disappears; **l**, the WB is blocked, and the intensity distribution is identical to **a**. Repeated switchings yield stable CS pairs at different locations, for current between 270 mA (sample centre below lasing threshold) and 320 mA (above threshold), thus showing that sample roughness pins the CSs but does not limit in principle the multiplicity of the structures' configurations.

designed a sample to minimize such a gradient and to maximize uniformity in parameter values across the whole section. It presents a central region where the gradient almost vanishes. The current crowding at the borders, with associated localized lasing, still exists. All other characteristics of the sample remain unchanged with respect to the first one. We repeat the experiments with the new sample, and we observe (Fig. 4a) that the homogeneous state can cover most of the diameter of the VCSEL; this occurs over an appreciable range of frequencies of the external field. A boundary is still observable between a pattern and the homogeneous state, on the left side of the sample. By injecting the writing beam inside the homogeneous state, we can generate a CS that remains when the writing beam is removed. We then apply this beam in a different location without changing any parameter value, and a second spot is generated. This spot will also persist after removal of the writing beam. We reach, then, the situation in which two CSs exist. Changing the phase of the writing beam and re-injecting it successively at the location of each spot, we erase each spot in an independent way. The full series is displayed in Fig. 4. In the experiment, the position of the CS can be changed by adding a weak gaussian beam (in phase with the holding beam and with a smaller waist) in a location lying up to three CS diameters off the soliton peak. After removal of this additional gaussian beam, the CS comes back to one of the previous positions.

The theoretical analyses and numerical simulations had the following features, yielding a consistent interpretation on the observed behaviour of CSs. When simulating the switch-on of a CS in the sample with small resonance gradient ($\nabla\theta$), the CS follows $\nabla\theta$, drifting leftwards until it merges with the pattern. The small intensity gradient of the gaussian holding beam alone is unable to counterbalance the drift. When a stochastic process simulating the sample roughness is accounted for, the CS moves to a location where it remains fixed. The conditions for such 'trapping' depend on the balance between the local resonance and $\nabla\theta$. The number and distribution of such 'trapping sites', related to the imperfections of the device, are interspersed densely enough to allow for a large number of stable CS locations throughout the sample. This effect of layer-related roughness is rather new to investigations[24]: it does not prevent CS motion under the influence of additional field gradients, so that CSs can be manipulated exactly as in the experiment. In particular, the CS drift can be governed by injecting a second gaussian beam with waist smaller than that of the holding beam, but larger than the CS radius. When this beam is positioned close to where the CS has been turned on, it attracts the CS towards its maximum, and traps it in a location where the pull induced by $\nabla\theta$ is balanced by the intensity gradient; this occurs in a range approximately on the order of the gaussian waist, in agreement with the experiment.

Using CSs, we have realized a monolithic two-bit all-optical information processor: we consider that these results open a possible way to developing a practical device. The future development of our results requires an increase in the number of CSs that can be simultaneously present, and also a way of inducing controllable motion of CSs. To achieve these goals, it will be necessary to introduce appropriate spatial modulations in the holding beam, and to further improve the homogeneity of the sample in the transverse plane. □

Received 5 June; accepted 1 August 2002; doi:10.1038/nature01049.

1. McDonald, G. S. & Firth, W. J. Switching dynamics of spatial solitary wave pixels. *J. Opt. Soc. Am. B* **10,** 1081–1089 (1993).
2. Brambilla, M., Lugiato, L. A. & Stefani, M. Interaction and control of optical localized structures. *Europhys. Lett.* **34,** 109–114 (1996).
3. Firth, W. J. & Scroggie, A. J. Optical bullet holes: robust controllable localized states of a nonlinear cavity. *Phys. Rev. Lett.* **76,** 1623–1626 (1996).
4. McLaughlin, D. W., Moloney, J. V. & Newell, A. C. Solitary waves as fixed points of infinite-dimensional maps in an optical bistable ring cavity. *Phys. Rev. Lett.* **51,** 75–78 (1983).
5. Rosanov, N. N. & Khodova, G. V. Autosolitons in bistable interferometers. *Opt. Spectrosc.* **65,** 449–450 (1988).
6. McDonald, G. S. & Firth, W. J. Spatial solitary wave optical memory. *J. Opt. Soc. Am. B* **7,** 1328–1335 (1990).
7. Tlidi, M., Mandel, P. & Lefever, R. Localized structures and localized patterns in optical bistability. *Phys. Rev. Lett.* **73,** 640–643 (1994).
8. Taranenko, V. B., Staliunas, K. & Weiss, C. O. Spatial soliton laser: localized structures in a laser with a saturable absorber in a self-imaging resonator. *Phys. Rev. A.* **56,** 1582–1591 (1997).
9. Saffman, M., Montgomery, D. & Anderson, D. Z. Collapse of a transverse-mode continuum in a self-imaging photorefractively pumped ring resonator. *Opt. Lett.* **19,** 518–520 (1994).
10. Weiss, C. O., Vaupel, M., Staliunas, K., Slekys, G. & Taranenko, V. B. Solitons and vortices in lasers. *Appl. Phys. B* **68,** 151–168 (1999).
11. Schreiber, A., Thuering, B., Kreuzer, M. & Tschudi, T. Experimental investigation of solitary structures in a nonlinear optical feedback system. *Opt. Commun.* **136,** 415–418 (1997).
12. Ramazza, P. L., Ducci, S., Boccaletti, S. & Arecchi, F. T. Localized versus delocalized patterns in a nonlinear optical interferometer. *J. Opt. B* **2,** 399–405 (2000).
13. Schaepers, B., Feldmann, M., Ackemann, T. & Lange, W. Interaction of localized structures in an optical pattern-forming system. *Phys. Rev. Lett.* **85,** 748–751 (2000).
14. Brambilla, M., Lugiato, L. A., Prati, F., Spinelli, L. & Firth, W. J. Spatial soliton pixels in semiconductor devices. *Phys. Rev. Lett.* **79,** 2042–2045 (1997).
15. Michaelis, D., Peschel, U. & Lederer, F. Multistable localized structures and superlattices in semiconductor optical resonators. *Phys. Rev. A* **56,** R3366–R3369 (1997).
16. Spinelli, L., Tissoni, G., Brambilla, M., Prati, F. & Lugiato, L. A. Spatial solitons in semiconductor microcavities. *Phys. Rev. A* **58,** 2542–2559 (1998).
17. Spinelli, L., Tissoni, G., Tarenghi, M. & Brambilla, M. First principle theory for cavity solitons in semiconductor microresonators. *Eur. Phys. J. D* **15,** 257–266 (2001).
18. Taranenko, V. B., Ganne, I., Kuszelewicz, R. & Weiss, C. O. Patterns and localized structures in bistable semiconductor resonators. *Phys. Rev. A* **61,** 063818-5 (2000).
19. Taranenko, V. B., Ganne, I., Kuszelewicz, R. & Weiss, C. O. Spatial solitons in a semiconductor microresonator. *Appl. Phys. B* **72,** 377–380 (2001).
20. Ackemann, T. *et al.* Spatial structure of broad area vertical-cavity regenerative amplifiers. *Opt. Lett.* **25,** 814–816 (2000).
21. Lugiato, L. A., Brambilla, M. & Gatti, A. *Advances in Atomic, Molecular and Optical Physics* (eds Bederson, B. and Walther, H.) **Vol. 40** 229–306 (Academic, Boston, 1998).
22. Thual, O. & Fauve, S. Localized structures generated by subcritical instabilities. *J. Phys.* **49,** 1829–1923 (1988).
23. Grabherr, M. *et al.* Bottom-emitting VCSEL's for high-CW optical output power. *IEEE Photon. Tech. Lett.* **10,** 1061–1063 (1998).
24. Fedorov, S. *et al.* Effects of spatial inhomogeneities on the dynamics of cavity solitons in quadratically nonlinear media. *Phys. Rev. E* **64,** 036610-8 (2001).

Acknowledgements We thank F. Capasso, P. Coullet, W. J. Firth and R. Kuszelewicz for discussions. This work was performed in the framework of the ESPRIT project PIANOS and the PRIN project 'Formazione e controllo di solitoni di cavità in microrisonatori a semiconduttore' of the Italian Ministry of University and Research, the contract ACI Photonique of the Ministere de l'Education et la Recherche de France, and the Project TIC99-0645-C05-02 of the Ministerio de Educación y Cultura, Spain.

Competing interests statement The authors declare that they have no competing financial interests.

Correspondence and requests for materials should be addressed to L.A.L. (e-mail: Luigi.Lugiato@uninsubria.it).

Stacking of conical molecules with a fullerene apex into polar columns in crystals and liquid crystals

Masaya Sawamura*‡, Kenji Kawai*, Yutaka Matsuo*, Kiyoshi Kanie†, Takashi Kato† & Eiichi Nakamura*

** Department of Chemistry, The University of Tokyo, Hongo, Bunkyo-ku, Tokyo 113-0033, Japan*
† Department of Chemistry and Biotechnology, School of Engineering, The University of Tokyo, Hongo, Bunkyo-ku, Tokyo 113-8656, Japan

Polar liquid crystalline materials can be used in optical and electronic applications, and recent interest has turned to formation strategies that exploit the shape of polar molecules and their interactions to direct molecular alignment[1,2]. For example, banana-shaped molecules align their molecular bent within smectic layers[3], whereas conical molecules should form polar

‡ Present address: Department of Chemistry, Hokkaido University, Kita-ku, Sapporo 060-0810, Japan.

